

Chapter 2

Processing of Star Catalog and Star Image

Processing of star catalog and star image is the groundwork for star identification. The star sensor process establishes the three-axis attitude of spacecraft by observing and identifying stars. Thus, star information is indispensable. The star information used by the star sensor process mainly includes the positions (right ascension and declination coordinates) and brightness of stars. Star sensor's onboard memory can store the basic information of stars within a certain range of brightness. And this simplified catalog is generally called Guide Star Catalog (GSC). To accelerate the retrieval of guide stars, partition of the star catalog usually has to be done, which plays an important role in enhancing star identification and star tracking. At the early design stage of the star image processing and star identification algorithms, simulation approaches have to be taken to verify their correctness and to conduct performance evaluation. Therefore, star image simulation lays the foundation for simulation research of the star sensor. The measuring accuracy of the star vector by star sensor directly reflects the star sensor's performance in attitude establishment. Meanwhile, the measuring accuracy of the star vector is closely linked to star sensor's performance quality in star centroiding accuracy. Thus, it is necessary to conduct research on highly accurate centroiding algorithms that can be used by the star sensor technique.

This chapter first introduces the composition of GSC and partition methods of the star catalog. It also discusses guide star selection and double star processing. Then, it introduces star image simulation and star centroiding. After this, it discusses the calibration of centroiding error.

2.1 Star Catalog Partition

Star catalog partition plays an important role in star identification. It can accelerate the retrieval of guide stars in the star catalog, speed up full-sky star identification

and star identification with established initial attitude. This section introduces GSC and catalog partition methods and presents star catalog partition with an inscribed cube method.

2.1.1 Guide Star Catalog

The number of stars in the star catalog has much to do with star magnitude. With the increase in star magnitude, the number of stars in the star catalog increases drastically. Through statistical analysis, an empirical equation regarding the relationship between the total number of stars distributed in the full sky and the change of star magnitude is obtained as follows [1]:

$$N = 6.57 \cdot e^{1.08 Mv} \tag{2.1}$$

N stands for the total number of stars distributed in the full sky. Mv stands for star magnitude. Table 2.1 shows different star magnitudes and their corresponding total numbers of stars in Star Catalog SAO J2000.

To meet the demand of star identification by star sensor method, stars brighter than (or whose Mv is less than) certain magnitude are selected from the standard catalog and then used to build a smaller catalog (GSC) that is appropriate for star identification. Stars selected in the GSC are called guide stars. GSC contains the basic information of a guide star: right ascension, declination, and magnitude. The selection of magnitude is related to the star sensor’s parameters. On the one hand, magnitude should be comparable to the limiting magnitude that can be detected by star sensor, that is, stars that can be observed by star sensor should be included in the GSC. Thus, magnitude should be equal to or slightly greater than the limiting magnitude that can be detected by star sensor, and the number of guide stars within the field of view must meet the needs of star identification. On the other hand, magnitude should be as small as possible on the premise that normal identification

Table 2.1 Different star magnitudes and their corresponding total numbers of stars

Magnitude	Total number of stars
3.0	155
3.5	260
4.0	480
4.5	871
5.0	1571
5.5	2859
6.0	5103
6.5	9040
7.0	15,935
7.5	26,584
8.0	46,172

can be achieved, which not only reduces the capacity of GSC, but also speeds up identification. Meanwhile, the probability of a redundant match drops with the decrease in the total number of guide stars. For example, if the limiting magnitude that can be detected by star sensor is 5.5 Mv, a total of 5103 stars whose brightness is greater than 6 Mv can be selected to make up a GSC.

2.1.2 Current Methods in Star Catalog Partition

How to retrieve guide stars rapidly must be taken into account in the process of building a GSC. The rapid retrieval of guide stars is of great importance in star identification, especially those in the tracking mode or with prior attitude information. If the arrangement of guide stars in a GSC is irregular, the entire GSC has to be traversed. Obviously, this kind of searching is rather inefficient. Therefore, the celestial area is usually divided into several sub-blocks.

Current methods in star catalog partition are listed below.

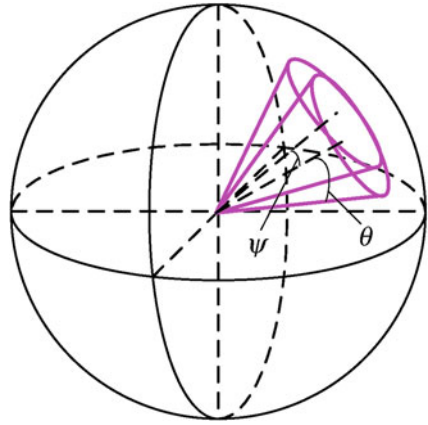
(1) Declination Zone Method

Through this method, the celestial sphere is divided into spherical zones (sub-blocks) by planes that are parallel to the equatorial plane. Each spherical zone has the same span of declination [2]. And guide stars in GSC can be directly retrieved by using a declination value. The problem with this method lies in the extremely uneven distribution of each sub-block. The number of guide stars in the sub-blocks near the equator is far greater than those near the celestial poles. This method does not make use of the information of right ascension, and the sub-blocks for retrieval contain a large number of redundant guide stars. Thus, its retrieval efficiency is rather low.

(2) Cone Method

Ju [3] divides the celestial sphere by using the cone method, as shown in Fig. 2.1. This method views the center of the celestial sphere as the vertex and uses 11,000 cones to divide the celestial sphere into regions that are exactly equivalent in size. When the angle (ψ) between the axes of neighboring cones is equal to 2.5° and the cone-apex angle (θ) is equal to 8.85° (the FOV is $10^\circ \times 10^\circ$), the stars included in the FOV by any boresight pointing are sure to be located within a certain cone. Through this method, possible matching stars that may correspond to measured stars in the FOV can be listed rapidly if the approximate boresight pointing of the star sensor is known beforehand. Since cones are overlapping, one measured star may be included in different sub-blocks. Thus, this partition method sets a high demand for storage space.

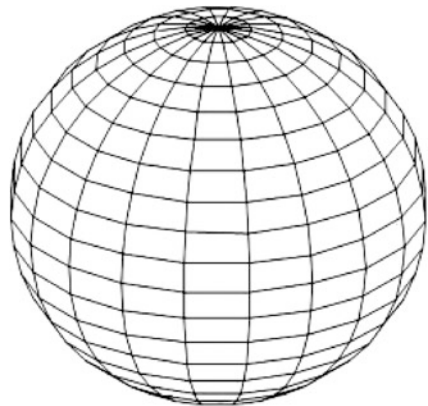
Fig. 2.1 Partition of the celestial area through cone method



(3) Sphere-Rectangle Method

Chen [4] uses the sphere-rectangle method to divide the celestial area. On the basis of a right ascension circle and declination circle, this method divides the celestial sphere into nonoverlapping regions, as shown in Fig. 2.2. The entire celestial area is divided into 800 sphere-rectangles and right ascension and declination are divided into 40 and 20 equal parts, respectively. Each sphere-rectangle stands for a span of 9° in the ascension direction and in the declination direction, respectively. It can be seen that this sphere-rectangle with right ascension and declination coordinates cannot be equal to the real FOV. The sizes of sphere-rectangles at different latitudes are different from each other, as shown in Fig. 2.2. In addition, the sub-blocks near the celestial poles cannot be completely represented by sphere-rectangles, so the retrieval of guide stars becomes consequently complicated. Since right ascension and declination coordinates are uneven themselves, the partition of the celestial sphere in that coordinate system cannot be even as well.

Fig. 2.2 Partition of the celestial area through sphere-rectangle method



2.1.3 Star Catalog Partition with Inscribed Cube Methodology

Zhang et al. [5, 6] use a completely different method. They divide the celestial area in the rectangular coordinate system and propose a star catalog partition with an inscribed cube method. This method realizes an even and nonoverlapping partition of the celestial area and the partition procedures are as follows.

- ① With inscribed cube, the celestial sphere is divided evenly into six regions, as shown in Fig. 2.3a. A cone is formed when the center of the celestial sphere is connected to the four vertices of each cube side, respectively. The cone is intersected with the celestial sphere and divides the sphere into six parts: S_1 – S_6 . The direction vectors of the central axis (v) of S_1 and its four boundary points are as follows:

$$\begin{aligned} v &= (0, 0, 1) \quad w_1 = (1, 1, 1)/\sqrt{3} \quad w_2 = (1, -1, 1)/\sqrt{3} \quad w_3 = (-1, -1, 1)/\sqrt{3} \quad w_4 \\ &= (-1, 1, 1)/\sqrt{3} \end{aligned} \quad (2.2)$$

And the direction vectors of the central axes (v) of S_2 – S_6 and their four boundary points can be analogized and so on.

- ② Each part of S_1 – S_6 can be further divided into $N \times N$ sub-blocks, as shown in Fig. 2.3b, c. In this way, the entire celestial sphere is divided into $6 \times N \times N$ sub-blocks. Besides, all sub-blocks are equivalent in size, the FOV

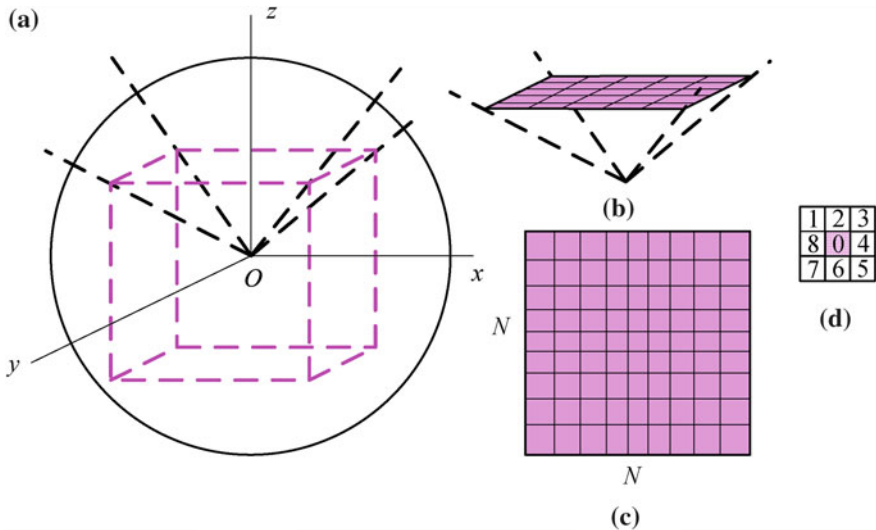


Fig. 2.3 Partition of the celestial area

being covered amounting to $90/N \times 90/N$. The direction vectors of each sub-block's central axis and boundary points can be acquired based on the direction vectors of S_1-S_6 .

Based on this method, the celestial sphere is divided. The GSC is scanned and each guide star finds its corresponding sub-block. After this, a partition table is created, as shown in Fig. 2.4.

The partition table has $6 \times N \times N$ parts, each representing a sub-block. Each part records the following information:

Index: index number of a sub-block

(x, y, z): direction vector of the central axis of a sub-block

Member num: the total number of stars in a sub-block

Member list: list of stars in a sub-block

Neighbor num: number of neighboring sub-blocks (as shown in Fig. 2.3d)

Neighbor list: list of neighboring sub-blocks.

(x, y, z) is arranged by its magnitude in ascending (or descending) order. If the direction vector of the boresight pointing (or right ascension and declination coordinates) is known beforehand, the corresponding sub-block and its neighboring sub-block can be found quickly in the celestial area. The index number of the sub-block to which a guide star is affiliated is also stored in the GSC in order to retrieve its neighboring guide star rapidly from its index number. Thus, the GSC contains the direction vector and magnitude of a guide star and the index number of the sub-block to which it is affiliated. The GSC and partition table created in that way can realize the rapid retrieval from initial attitude (boresight pointing) or guide star index number to guide stars in a given neighborhood.

Take the FOV of $10^\circ \times 10^\circ$, for example. In order to make any sub-block and its neighboring sub-blocks (such as the 3×3 sub-blocks in Fig. 2.3d) incorporate the

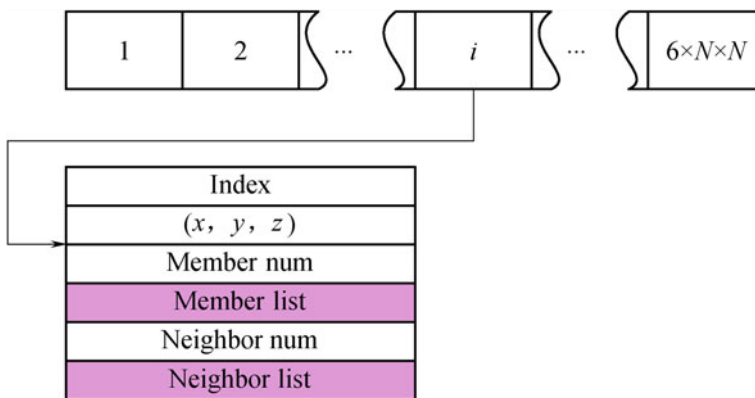


Fig. 2.4 Structure of the partition table

FOV as completely as possible, take $N = 9$, that is, divide the celestial area into $6 \times 9 \times 9 = 486$ sub-blocks and the size of each sub-block is $10^\circ \times 10^\circ$. Then there is no need to traverse the entire GSC to retrieve guide stars and the average search scope is only $9/486 = 1/54$ that of before. After partition, the statistical results of the number of guide stars distributed in each sub-block are as follows:

- the maximum number is 39;
- the minimum number is 2;
- the average number is 10.61.

2.2 Guide Star Selection and Double Star Processing

Guide star selecting is aimed at cutting down the number of guide stars as much as possible on the premise that correct star identification is guaranteed, which not only reduces the storage capacity required in star identification algorithms, but also speeds up star identification. It is thus an important work for enhancing star identification and reducing the capacity of the navigation database. Meanwhile, double star processing has implications for star identification. This section introduces guide star selecting and discusses the processing methods of a double star.

2.2.1 Guide Star Selection

Assume that guide stars are distributed evenly and randomly in the celestial area, the number of stars in the FOV approximately follows a poisson distribution [7]:

$$p(X = k) = \frac{\mu^k e^{-\mu}}{k!} \tag{2.3}$$

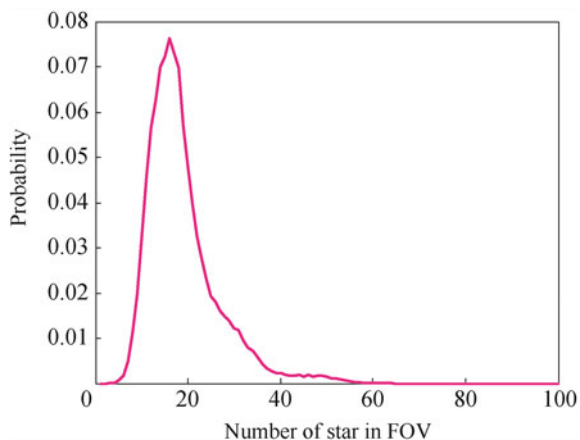
μ can be computed as follows: the spherical area of an FOV of $12^\circ \times 12^\circ$ is 0.04376 and the number of FOV accommodated by the entire celestial sphere is $4\pi/0.04376 = 287.02$. Thus, the average number of stars whose brightness is greater than 6 Mv in each FOV is 17.78 ($\mu = 5103/287.02 = 17.78$).

Based on Poisson distribution, the probability of the number of stars in the FOV is shown in Table 2.2.

Table 2.2 Probability of the number of stars in the FOV based on Poisson distribution (FOV of $12^\circ \times 12^\circ$, Magnitude ≥ 6)

	$X \leq 2$	$X \leq 5$	$X \leq 10$	$X \geq 20$	$X \geq 30$	$X \geq 40$	$X \geq 50$
Probability P (%)	0	0.04	3.38	32.97	0.50	0	0

Fig. 2.5 Probability statistics of the distribution of guide stars in the FOV (FOV of $12^\circ \times 12^\circ$, Magnitude ≥ 6)



The statistical result (as shown in Fig. 2.5) shows the numbers of stars brighter than 6 Mv in an FOV of $12^\circ \times 12^\circ$ by 100,000 random boresight pointings. The maximum number of stars in the FOV is 63, the minimum number is 2, and the average number is 17.8. The results computed by Poisson distribution are basically the same as the simulation results, as shown in Fig. 2.5. In fact, the distribution of stars in the celestial sphere is not even or random: the distribution near the celestial pole is sparse while that near the equator is relatively dense.

As for star identification, the number of measured stars in the FOV cannot be too small and must meet the minimum requirements of identification (≥ 3). If the number is too small, then the information that can be used would be relatively little and, thus, it would be difficult for identification. Meanwhile, accuracy e in attitude establishment is related to the number n of stars that are involved in attitude establishment in the FOV:

$$e = e_0 / \sqrt{n} \quad (2.4)$$

Here, e_0 is the accuracy in attitude establishment of one star. Theoretically, the larger n is, the higher the accuracy in attitude establishment would be. Thus, in order to guarantee high accuracy in attitude establishment, the average number of stars in the FOV should not be too small. Generally, $n \geq 5-6$.

Correspondingly, the number of guide stars in each FOV should meet the needs of normal identification and attitude establishment. It can be noted that the number of stars in the FOV is relatively larger in some celestial areas where stars are densely distributed. Generally, excessive stars do not affect the results of identification and contribute little to the enhancement of accuracy in attitude establishment. In contrast, excessive stars mean more time in identification and a larger capacity of GSC and pattern database. In addition, excessive stars lead to too many redundant matches. Thus, the number of guide stars in the FOV should be as small as possible on the premise that normal identification and accuracy in attitude establishment can

be guaranteed, that is, redundant guide stars should be eliminated in dense celestial areas in order to guarantee that the distribution of guide stars in the entire celestial area is as even as possible.

Based on the single magnitude threshold, there are too many stars in the FOV as a result of some boresight pointings, while there are no stars in the FOV of some celestial areas. Obviously, this method cannot guarantee the even distribution of selected guide stars in the celestial area. Based on the process of partition of GSC, guide star selection can be realized by traversing the distribution of guide stars in the full sky.

As described in the last section, the celestial area is divided into $6 \times 9 \times 9 = 486$ sub-blocks and then the direction vector of each sub-block's corresponding central axis can be obtained. 486 boresight pointings (direction vector) evenly distributed in the full sky resulting from this method and the angle between each pair of neighboring boresight pointings is 10° . Similarly, the full sky can be divided into $6 \times 100 \times 100 = 60,000$ boresight pointings that are evenly distributed, and the angle between each pair of neighboring boresight pointings is 0.9° . The 60,000 boresight pointings are scanned, and then guide stars located within the FOV (such as a circular FOV) by each boresight pointing are established.

If the number of guide stars in the FOV is lower than or equal to a certain threshold number C , then no processing is needed. Otherwise, it is necessary to arrange guide stars in the order of brightness (magnitude), keeping the brightest C stars and eliminating darker ones. The selection of C is related to the requirements put forth by star identification for the minimum number of guide stars in the FOV and accuracy in attitude establishment.

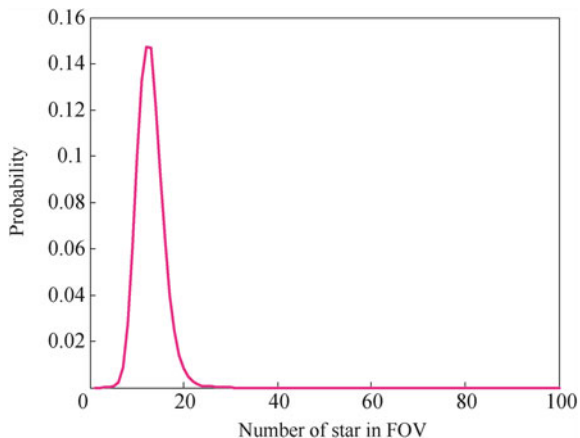
This method mainly takes into account the characteristic that brighter stars are easier to be sensitized by the star sensor method. Thus, it is reasonable to view brighter stars as guide stars. In the relatively dense celestial areas, redundant darker stars can be eliminated from GSC, while in the relatively sparse celestial areas, as many as possible guide stars should be retained.

Take $C = 6$, and Fig. 2.6 shows the probability statistics of the number of guide stars in the FOV after selecting. The minimum number of guide stars in the FOV is 2, the maximum number is 28, and the average number is 11.9. After selection, the total number of guide stars drops from 5103 to 3360. Compared with Fig. 2.5, Fig. 2.6 shows that the distribution of guide stars is more reasonably even than that before selection.

2.2.2 Double Star Processing

“Double star” is a different concept from that of “binary star” in astronomy. Astronomically, binary stars are two stars that are close to and revolve around each other. By contrast, here ‘double star’ means two stars that seem to be close in the direction of the line of sight (actually they may be far away from each other), and

Fig. 2.6 Probability statistics of the distribution of guide stars in the FOV after selecting (FOV $12^\circ \times 12^\circ$, Magnitude ≥ 6)



the star spots formed by the two on the image plane of the star sensor cannot be separated from each other. The size of a star spot is related to the point spread function (PSF) of the optical system and its visual magnitude.

Generally, in order to improve the accuracy of the star position, a defocusing technique is often used to make the size of the image point range from 3×3 to 5×5 pixels. Assume the radius of PSF is one pixel, Fig. 2.7a, b show the gray distribution of the double star's spot images. Star spot images can be approximately represented by the Gaussian function:

$$f(x, y) = A \exp\left(-\frac{(x - x_0)^2 + (y - y_0)^2}{2\sigma^2}\right) \quad (2.5)$$

A stands for the brightness of stars which is related to magnitude. Assume the binary threshold in the process of star spot extraction is T . The minimum distance between two stars to constitute double star must be d , as shown in Fig. 2.7c.

$$T = 2A \exp\left(-\frac{(d/2)^2}{2\sigma^2}\right) \quad (2.6)$$

Take $T = 80$, $\sigma = 1$ and $A = 255$. By computation, $d \approx 4$. Thus, two stars whose star spot positions are smaller than four pixels apart in the image plane are viewed as a double star. This means that two guide stars between which the angular distance is smaller than 0.047° (e.g., $12^\circ \times 12^\circ$ in FOV, 1024×1024 in resolution) are treated as a double star.

A double star interferes in the process of star identification and, thus, general star identification algorithms cannot find correct matches for a double star. Meanwhile, a double star affects the identification of other stars. The traditional way of

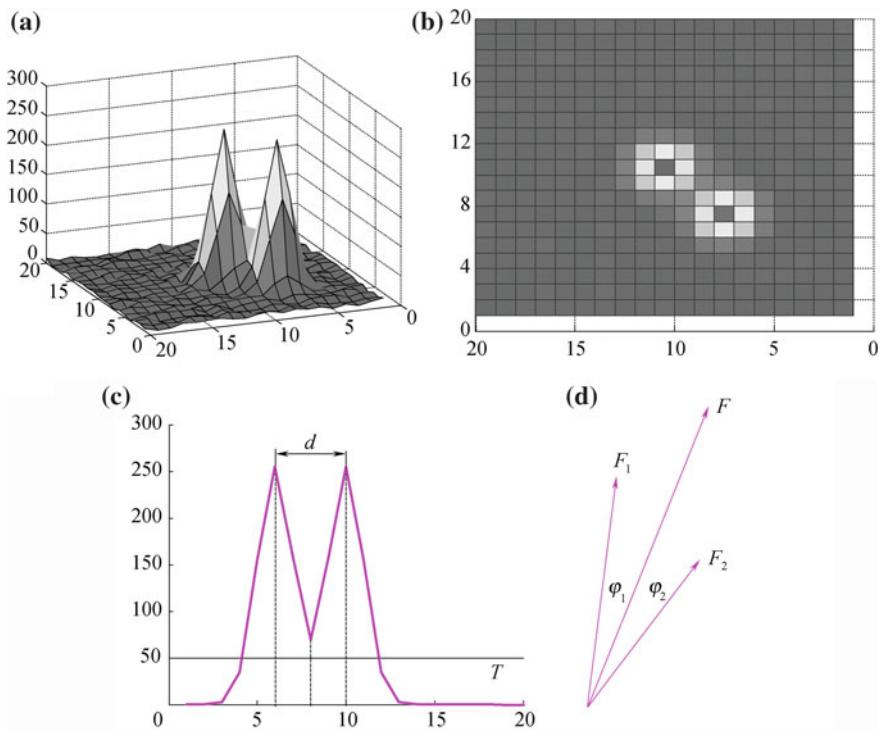


Fig. 2.7 Double star and double star processing

processing a double star is to eliminate them directly, which is feasible when the number of stars in the FOV is quite large. When the number of stars in the FOV is relatively small, eliminating the double star directly means throwing away some available information that is necessary for star identification. Considering that, the double star can be treated as a new “synthetic star” whose magnitude and orientation are synthesized by those of the double star. In fact, star spot images of the double star acquired by star sensor can be viewed as synthesized by the star spot images of the two stars.

Assume the magnitude of each of the double star is m_1 and m_2 , respectively, and the direction vector of each is v_1 and v_2 , as shown in Fig. 2.7d. Star’s brightness is represented by the density of optical flow, and the brightness ratio of the two stars is:

$$\frac{F_1}{F_2} = e^{(m_2 - m_1)/2.5} \quad (2.7)$$

The brightness of the synthetic star can be viewed as the synthesis of that of the two stars that constitute the double star, that is,

$$F = F_1 + F_2 \quad (2.8)$$

Thus,

$$\frac{F}{F_2} = \frac{F_1 + F_2}{F_2} = e^{(m_2 - m)/2.5} \quad (2.9)$$

And the magnitude of the synthetic star is:

$$m = m_2 - 2.5 \log \left(1 + \frac{F_1}{F_2} \right) = m_2 - 2.5 \log \left(1 + e^{(m_2 - m_1)/2.5} \right) \quad (2.10)$$

Assume the angular distance between the synthetic star and each of the double stars is φ_1 and φ_2 , respectively, and the angular distance between the two stars is φ .

$$F_1 \varphi_1 = F_2 \varphi_2$$

$$\varphi = \varphi_1 + \varphi_2 = \varphi_1 \left(1 + \frac{F_1}{F_2} \right) = \varphi_1 \left(1 + e^{(m_2 - m_1)/2.5} \right) \quad (2.11)$$

Thus, φ_1 and φ_2 can be computed, and the direction vector (v) of the synthetic star can be obtained:

$$\begin{aligned} v \sin \varphi &= v_1 \sin \varphi_1 + v_2 \sin \varphi_2 \cong v_1 \varphi_1 + v_2 \varphi_2 \\ v &= (v_1 \varphi_1 + v_2 \varphi_2) / \sin \varphi \end{aligned} \quad (2.12)$$

2.3 Star Image Simulation

There are mainly three approaches in star identification algorithm research: digital simulation, hardware-in-the-loop simulation, and field test of star observation. These three approaches correspond to three different stages in designing a star sensor and a star identification algorithm. At the early design stage, preliminary performance evaluation of the algorithm was done using digital simulation to determine appropriate identification parameters. Digital simulation is computer-based and is involved in the whole process of star image simulation, star image processing, and star identification. After the design of the star sensor finishes, star identification algorithms can be verified using the method of hardware-in-the-loop simulation.

Through hardware-in-the-loop simulation, star field simulator (SFS) generates star images. Then the imaging, processing, and identification of those generated star images are done by star sensor. Field tests of star observation are done during the night. Star images are photographed and then identified by the star sensor method in order to further verify the star identification algorithms. As for star identification algorithms, star image simulation is the fundamental work of the research. That is, when star sensor's attitude or boresight pointing is given, those star images photographed by star sensor can be simulated. Star image simulation mainly includes two processes: the imaging of star sensor and the synthesis of digital star images.

2.3.1 The Image Model of the Star Sensor

In the transformation of coordinates in the process of star image simulation, it is necessary to involve the celestial coordinate system, the star sensor coordinate system and the star sensor image coordinate system. The simple definitions of these coordinate systems are as follows [5]:

- ① Celestial coordinate system: With the celestial equator as its fundamental circle, the hour circle passing through the vernal equinox as its primary circle and the vernal equinox as its principal point, as shown in Fig. 1.2, this system uses right ascension and declination as its coordinates.
- ② Star sensor coordinate system: this is a system with the projection center o (the point on the boresight, with its distance from the focal plane as f , is called the optical center) as the origin of coordinates, boresight as z axis, and two straight lines that pass through point o and are parallel to both sides of the image sensor as the x and y axes. Figure 2.8 shows the front projection imaging of star sensor.
- ③ Image coordinate system: this system is a plane coordinate system of x and y axes that are parallel to both sides of the image sensor, with the center (principal point) of image sensor as the origin of the coordinates, as shown in Fig. 2.8.

Assume the coordinate of a star in the celestial coordinate system is (α_i, δ_i) , the direction vector in the star sensor coordinate system is (x_i, y_i, z_i) , and the coordinate of the imaging point in the image coordinate system is (X_i, Y_i) .

The imaging process of star sensor consists of two steps: the rotation transformation of stars from the celestial coordinate system to the star sensor coordinate system and the perspective projection transformation from the star sensor coordinate system to the image coordinate system [5].

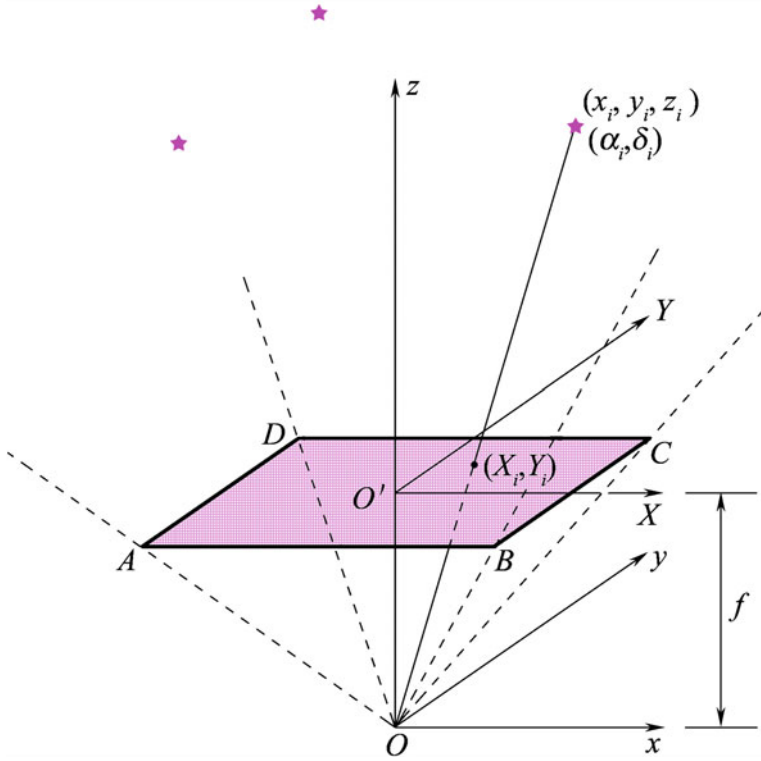


Fig. 2.8 Illustration of the star sensor coordinate system, the image coordinate system, and front projection imaging

(1) Rotation Transformation

Assume the attitude angle of the star sensor is $(\alpha_0, \delta_0, \phi_0)$. Here, α_0 stands for right ascension, δ_0 for declination, and ϕ_0 for roll angle. The rotation matrix (M) from the star sensor coordinate system to the celestial coordinate system can be expressed as:

$$M = \begin{pmatrix} \cos(\alpha_0 - \pi/2) & -\sin(\alpha_0 - \pi/2) & 0 \\ \sin(\alpha_0 - \pi/2) & \cos(\alpha_0 - \pi/2) & 0 \\ 0 & 0 & 1 \end{pmatrix} \begin{pmatrix} 1 & 0 & 0 \\ 0 & \cos(\delta_0 + \pi/2) & -\sin(\delta_0 + \pi/2) \\ 0 & \sin(\delta_0 + \pi/2) & \cos(\delta_0 + \pi/2) \end{pmatrix}$$

$$\begin{pmatrix} \cos \phi_0 & -\sin \phi_0 & 0 \\ \sin \phi_0 & \cos \phi_0 & 0 \\ 0 & 0 & 1 \end{pmatrix} = \begin{pmatrix} a_1 & a_2 & a_3 \\ b_1 & b_2 & b_3 \\ c_1 & c_2 & c_3 \end{pmatrix} \quad (2.13)$$

In this matrix,

$$\begin{aligned}
 a_1 &= \sin \alpha_0 \cos \varphi_0 - \cos \alpha_0 \sin \delta_0 \sin \varphi_0 \\
 a_2 &= -\sin \alpha_0 \sin \varphi_0 - \cos \alpha_0 \sin \delta_0 \cos \varphi_0 \\
 a_3 &= -\cos \alpha_0 \cos \delta_0 \\
 b_1 &= -\cos \alpha_0 \cos \varphi_0 - \sin \alpha_0 \sin \delta_0 \sin \varphi_0 \\
 b_2 &= \cos \alpha_0 \sin \varphi_0 - \sin \alpha_0 \sin \delta_0 \cos \varphi_0 \\
 b_3 &= -\sin \alpha_0 \cos \delta_0 \\
 c_1 &= \cos \alpha_0 \sin \varphi_0 \\
 c_2 &= \cos \alpha_0 \cos \varphi_0 \\
 c_3 &= -\sin \delta_0
 \end{aligned}$$

Since M is an orthogonal matrix, the rotation matrix from the celestial coordinate system to the star sensor coordinate system can be expressed as $M^{-1} = M^T$. First, search image able stars with a circular FOV, and the right ascension and declination coordinates (α, δ) of stars that can be imaged on the image sensor should satisfy the following conditions:

$$\begin{aligned}
 \alpha &\in (\alpha_0 - R/\cos \delta_0, \alpha_0 + R/\cos \delta_0) \\
 \delta &\in (\delta_0 - R, \delta_0 + R)
 \end{aligned} \tag{2.14}$$

Here, R stands for the radius of a circular FOV (R is half of the diagonal angular distance of the FOV, for example, the value of R in an FOV of $12^\circ \times 12^\circ$ is equal to $6\sqrt{2}$ ($R = 6\sqrt{2}$). (α_0, δ_0) stands for the boresight pointing of star sensor. The direction vector of stars that satisfy Eq. (2.13) in the star sensor coordinate system can be expressed as:

$$\begin{pmatrix} x_i \\ y_i \\ z_i \end{pmatrix} = M^T \begin{pmatrix} \bar{x}_i \\ \bar{y}_i \\ \bar{z}_i \end{pmatrix} \tag{2.15}$$

Here, $\begin{pmatrix} \bar{x}_i \\ \bar{y}_i \\ \bar{z}_i \end{pmatrix} = \begin{pmatrix} \cos \alpha_i \cos \delta_i \\ \sin \alpha_i \cos \delta_i \\ \sin \delta_i \end{pmatrix}$ is the direction vector of stars in the celestial coordinate system.

(2) Perspective Projection Transformation

The imaging process of stars on the image sensor can be represented by the perspective projection transformation, as shown in Fig. 2.8. After perspective projection, the coordinates of stars' imaging points are as follows:

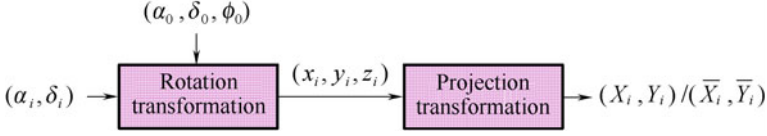


Fig. 2.9 Imaging process of star sensor

$$\begin{aligned} X_i &= f \frac{x_i}{z_i} = f \frac{a_1 \bar{x}_i + b_1 \bar{y}_i + c_1 \bar{z}_i}{a_3 \bar{x}_i + b_3 \bar{y}_i + c_3 \bar{z}_i} \\ Y_i &= f \frac{y_i}{z_i} = f \frac{a_2 \bar{x}_i + b_2 \bar{y}_i + c_2 \bar{z}_i}{a_3 \bar{x}_i + b_3 \bar{y}_i + c_3 \bar{z}_i} \end{aligned} \quad (2.16)$$

To sum up, the imaging process of star sensor can be illustrated by Fig. 2.9. The imaging model of star sensor can be expressed as follows:

$$s \begin{bmatrix} X \\ Y \\ 1 \end{bmatrix} = \begin{bmatrix} f & 0 & u_0 \\ 0 & f & v_0 \\ 0 & 0 & 1 \end{bmatrix} \cdot \begin{bmatrix} r_1 & r_2 & r_3 \\ r_4 & r_5 & r_6 \\ r_7 & r_8 & r_9 \end{bmatrix} \cdot \begin{bmatrix} \cos \beta \cos \alpha \\ \cos \beta \sin \alpha \\ \sin \beta \end{bmatrix} \quad (2.17)$$

In the above equation, s stands for nonzero scale factor, f for focal length of the optical system, (u_0, v_0) for optical center (the coordinates of the principal point), (r_1-r_9) for transformation matrix from the celestial coordinate system to the star sensor coordinate system, and (α, β) for the right ascension and declination coordinates of the starlight vector in the celestial coordinate system. Equation (2.17) shows that the position coordinates (α, β) of stars in the celestial coordinate system (world coordinate system) are in a one-to-one correspondence with the positions (X, Y) of image points on the image plane of star sensor.

(3) Nonlinear Model

In fact, an actual optical lens cannot achieve perfect perspective imaging, but has different degrees of distortion. As a result, the image of the spatial point is not located at the position (X, Y) as described by the linear model, but within the actual image plane coordinates (X', Y') migrated due to the distortion of the optical lens.

$$\begin{cases} X' = X + dx \\ Y' = Y + dy \end{cases} \quad (2.18)$$

Here, dx and dy stand for distortion values which are related to the position of the star spot's coordinates in the image. Generally, there exist radical and tangential distortions in an optical lens. As for three-order radical distortion and two-order tangential distortion, distortions in the directions of x and y can be expressed as follows [8]:

$$\begin{cases} dx = \bar{x}(q_1 r^2 + q_2 r^4 + q_3 r^6) + [p_1(r^2 + 2\bar{x}^2) + 2p_2\bar{x}\bar{y}](1 + p_3 r^2) \\ dy = \bar{y}(q_1 r^2 + q_2 r^4 + q_3 r^6) + [p_2(r^2 + 2\bar{y}^2) + 2p_1\bar{x}\bar{y}](1 + p_3 r^2) \end{cases} \quad (2.19)$$

Here, \bar{x} , \bar{y} and r can be defined as follows:

$$\begin{cases} \bar{x} = X - u_0 \\ \bar{y} = Y - v_0 \\ r^2 = \bar{x}^2 + \bar{y}^2 \end{cases} \quad (2.20)$$

To sum up, in the imaging model of the star sensor, linear model parameters f , (u_0, v_0) and nonlinear distortion coefficient $(q_1, q_2, q_3, p_1, p_2, p_3)$ constitute the intrinsic parameters of star sensor, while (r_1-r_9) makes up the extrinsic parameter.

In order to conduct a subsequent performance evaluation of the identification rate of the star identification algorithms, a certain level of positional noise (a gauss noise with mean = 0 and variances σ_x, σ_y) is added to the coordinates of the star spot image on the focal plane of the star sensor in a star image simulation so as to simulate centroid error.

2.3.2 The Composition of the Digital Star Image

For star sensor, the star can be viewed as a point light source. The positioning accuracy of a single pixel cannot meet the demand for attitude establishment. Thus, defocusing is often used to make the star spot image spread to multiple pixels, and then centroiding methods are used to obtain sub-pixel positioning accuracy [1]. The pixel size of the star spot is not only related to a star's brightness (magnitude), but also related to the PSF of the optical system. The gray distribution of a star spot image follows the PSF of the optical system and can be approximately represented by a two-dimensional Gaussian distribution function:

$$\mu_i(x, y) = \frac{1}{\sqrt{2\pi}\sigma} \exp\left(-\frac{(x - \bar{X}_i)^2 + (y - \bar{Y}_i)^2}{2\sigma^2}\right) \quad (2.21)$$

Assume that there are N stars in the star image, and a photoelectron density that is formed in the imaging process of target star spot can be expressed as follows [9]:

$$s(x, y) = \sum_{i=1}^N k \int s_i A \tau(\lambda) Q \mu_i(x, y) P(\lambda) t_s d\lambda \quad (2.22)$$

Here, k stands for bandwidth impact factor, A for optical entrance pupil area, $\tau(\lambda)$ for optical transmittance, and Q for quantum efficiency. $P(\lambda)$ stands for the spectral response of the imaging device and t_s for integration time.

$$s_i = 5 \times 10^{10} / 2.512^{M_i}.$$

In the above equation, M_i stands for the magnitude of the i -th star.

The photoelectron density that is formed in the process of background imaging can be expressed as follows:

$$b = \int b_0 A \tau(\lambda) P(\lambda) A_p t_s d\lambda \quad (2.23)$$

Here, $b_0 = 5 \times 10^{10} / 2.512^{M_b}$, M_b stands for the magnitude order of the background which can be generally of brightness of 10.0 Mv. A_p stands for angle area of a single pixel.

Thus, the total number of photoelectrons acquired by the (m, n) -th pixel ($0 \leq m < M$, $0 \leq n < N$) on the photosensitive surface is as follows:

$$I(m, n) = \int_{m dx}^{(m+1) dx} \int_{n dy}^{(n+1) dy} (s(x, y) + b) dx dy \quad (2.24)$$

Integrate Eqs. (2.22) and (2.23), and then the above equation can be simplified as:

$$I(m, n) = \int_{m dx}^{(m+1) dx} \int_{n dy}^{(n+1) dy} \sum_{i=1}^N \frac{C}{2.512^{M_i}} \exp\left(-\frac{(x - \bar{X}_i)^2 + (y - \bar{Y}_i)^2}{2\sigma^2}\right) dx dy + B \quad (2.25)$$

Here, both B and C are constants.

In addition to the background and star spot, the final star image should also include noise signal which mainly consists of shot noise and the dark current noise of the image device. The white noise model can be represented by the random number of Gaussian distribution:

$$N(m, n) = \text{normrand}(0, \sigma_N) \quad (2.26)$$

Thus, the final output of the image signal can be expressed as follows:

$$P(m, n) = I(m, n) + N(m, n) \quad (2.27)$$

Table 2.3 Simulation parameters of star image

	Parameter values
Pixel resolution	1024 × 1024
Pixel size	12 μm × 12 μm
Position of the principal point	(512,512)
Focal length of optical system	58.4536 mm
FOV	12° × 12°
Maximum magnitude sensitized	6 Mv
Radius of PSF	1 pixel

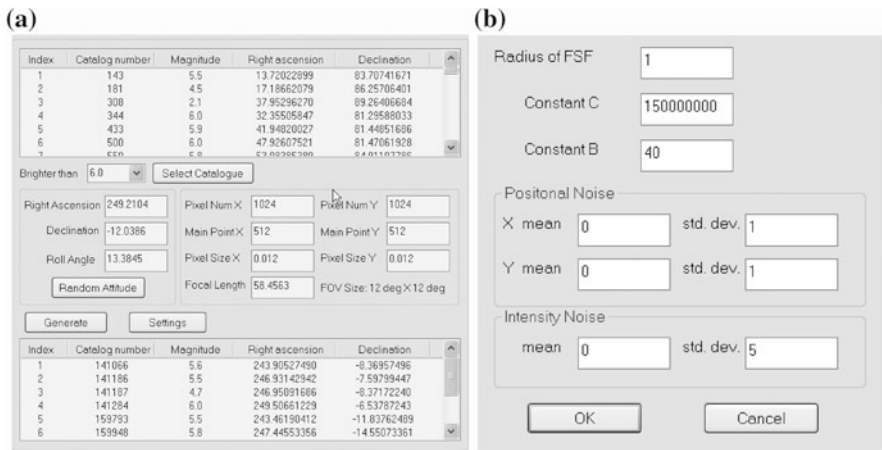


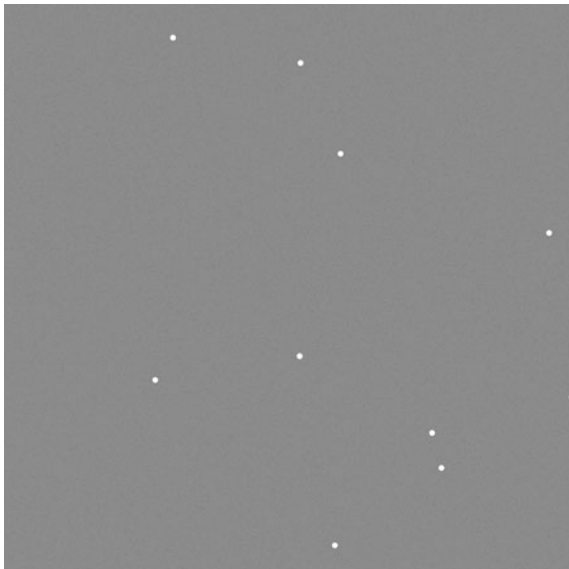
Fig. 2.10 Parameter setting in star image simulation

The parameters used in the process of star image simulation are shown in Table 2.3. In the process of image synthesis, parameters B , C , σ_x , σ_y , and σ_N can take the appropriate values as required based on the design specifications of the optical system and image device as shown in Fig. 2.10a, b. Figure 2.11 is a star image simulated when the attitude angle of star sensor is (249.2104, -12.0386, 13.3845).

2.4 Star Spot Centroiding

Restricted by the manufacturing technology of the imaging device, image resolution cannot be improved indefinitely. Thus, the method of increasing positioning accuracy by improving image resolution is limited. However, the method of image processing carried out by using software to conduct star spot centroiding is

Fig. 2.11 Simulated star images



effective. This section begins with an introduction to the preprocessing of the star image, discusses star spot centroiding methods and finally concludes with simulations and results analysis.

2.4.1 Preprocessing of the Star Image

A salient feature of low-level processing of a star image is the large amount of data. Take the eight-bit gray image with 1024×1024 resolution for example. The amount of data in each frame is 1 MB. Thus, in order to achieve real-time processing, the low-level processing algorithms of the star image must not be too complex. Meanwhile, considering the requirement that the low-level processing of a star image be achieved by adopting specific hardware circuit (e.g., FPGA or ASIC), the algorithms must also be characterized by parallel processing as much as possible. Preprocessing of the star image mainly includes noise removal processing and rough judgment of the stars.

The output of the image sensor is done via an image capture circuit. The original digital image signal obtained in this way is mixed with a lot of noises. Thus, noise removal processing of the original star image is generally done first. The common noise removal processing can use 3×3 or 5×5 low-pass filter template, for example, neighborhood average template and a Gauss template. To reduce the amount of computation of the algorithms, 3×3 low-pass filter template is often used.

Before extracting the information of star spot positions, the target star spots in the star image must be roughly judged. Rough judgment is actually a process of image segmentation which can be divided into two stages:

- ① separating the target star spot from the background;
- ② separating a single target star spot from others.

At the first stage, global threshold or local threshold can be used to segment the image. Generally, considering the characteristics of the star image and the complexity of algorithms, just one fixed global background threshold can be used to separate the star spot from the background. The selection of the global threshold can adopt multi-window sampling, i.e., selecting several windows randomly in the image, computing the mean of their gray distribution, and then taking this value as the mean of the background's gray distribution. Generally, the background mean plus five times the standard deviation of noise can be treated as the global background threshold [1].

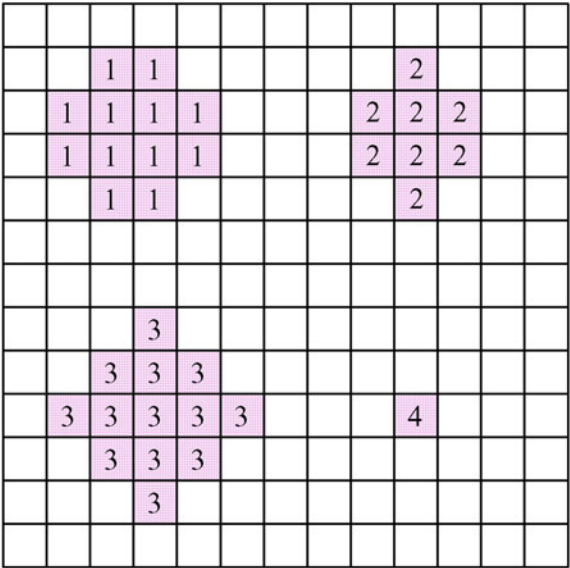
How to separate one target star spot from another, is a problem in the preprocessing of a star image. Ju [3] uses multi-threshold clustering to conduct clustering identification of the pixels whose gray value is greater than the global background threshold. The specific procedures are as follows:

- ① Set ten thresholds, group the pixels whose gray value is greater than the global background threshold together into the corresponding interval based on their gray values, and then put them in order.
- ② Each interval is scanned in descending order, the pixel with the maximum gray value is found in the current interval, and its neighborhood spot is sought out. They are regarded as belonging with the same star.

This method is relatively complex and involves a sorting operation. Considering the specific requirement for speed in star image processing, binary image processing can be used for reference, and then the connected domain algorithms [10] can be used to achieve a clustering judgment of the star spot. And the specific procedures are as follows:

- ① The image is scanned from left to right, top to bottom.
- ② If the gray value of a pixel is greater than background threshold (T), then:
 - * If there is a marker in the above or left spots, copy this marker.
 - * If there is the same marker in the above or left spots, copy this marker.
 - * If there are different markers in the above or left spots, copy the marker of the above spots and then the two markers are put into the equivalent table as an equivalent marker.
 - * Otherwise, allocate a new marker to this pixel and put it into the equivalent table.
- ③ Repeat step ② until all the pixels whose gray value is greater than T are scanned.

Fig. 2.12 Connected domain segmentation algorithms



- ④ Combine the pixels with the same marker in the equivalent table and reallocate a marker with a lower index number to them.

After the segmentation based on connected domains algorithm, each star spot is represented by a set of neighboring pixels with the same marker, for example, spots 1, 2, 3 in Fig. 2.12. To eliminate the influence of potential noise interference, star spots whose number of pixels is lower than a certain threshold should be abandoned, for example, spot 4 in Fig. 2.12. As can be seen from the above procedures, threshold segmentation and connected domain segmentation algorithms can be done at the same time. Thus, the image can be scanned just once, which is very suitable for realization by a specific hardware circuit and can meet real-time demands [11].

2.4.2 Centroiding Methods

Generally, many current centroiding methods can achieve sub-pixel (or even higher) accuracy. To obtain higher accuracy in star spot positions from the star image, defocusing is often used to make the imaging points of stars on the photosensitive surface of image sensor spread to multiple pixels. Both theoretical derivations and experiments prove that ideal centroiding accuracy can be achieved when the diameter of dispersion circle ranges from three to five pixels [12, 13].

There are two categories of centroiding methods for spot-like image: the one based on gray and the one based on edge [14]. The former often uses the

information of spot's gray distribution, for example, centroid method, surface fitting method, etc. The latter often uses the information of a spot's edge shape, for example, edge circle (ellipse) fitting, Hough transformation, etc. The former applies to relatively small spots with an even distribution of gray, while the latter applies to larger spots that are less sensitive to gray distribution. Generally, the diameter of spot star spots in the actual measured star image ranges from three to five pixels and their gray values approximately follow a Gaussian distribution. Thus, for target star spots, it is more appropriate to adopt the methods based on gray to conduct centroiding processing. Simulation experiments also show that the accuracy of this method is higher than that of the method based on the edge method. Here, the former is mainly introduced, including the centroid method, the modified centroid method and the Gaussian surface fitting method. Then their positioning accuracy is analyzed.

(1) Centroid Method

Assume the image that contains target star spots is represented by $f(x, y)$. Here,

$$x = 1, \dots, m, \quad y = 1, \dots, n.$$

The process of thresholding is as follows:

$$F(x, y) = \begin{cases} f(x, y) & f(x, y) \geq T \\ 0 & f(x, y) < T \end{cases} \quad (2.28)$$

In the above equation, T stands for background threshold. Centroid method is actually the first moment of the image after thresholding:

$$x_0 = \frac{\sum_{x=1}^m \sum_{y=1}^n F(x, y)x}{\sum_{x=1}^m \sum_{y=1}^n F(x, y)}, \quad y_0 = \frac{\sum_{x=1}^m \sum_{y=1}^n F(x, y)y}{\sum_{x=1}^m \sum_{y=1}^n F(x, y)} \quad (2.29)$$

The centroid method is the most commonly used. It is easy to realize with a relatively high positioning accuracy. It requires that the gray distribution of the spot image be relatively even. It has some modified forms, including a centroid method including a threshold and square weighting centroid method.

(2) Square Weighting Centroid Method

The computational equation of the square weighting centroid method can be expressed as follows:

$$x_0 = \frac{\sum_{x=1}^m \sum_{y=1}^n F^2(x, y)x}{\sum_{x=1}^m \sum_{y=1}^n F^2(x, y)}, \quad y_0 = \frac{\sum_{x=1}^m \sum_{y=1}^n F^2(x, y)y}{\sum_{x=1}^m \sum_{y=1}^n F^2(x, y)} \quad (2.30)$$

The square weighting centroid method substitutes the square of the gray value for the gray value expressed as weight. It highlights the influence of the pixel which is closer to the center and with a relatively large gray value on the central position.

(3) Centroid Method with Threshold

$F(x, y)$ in Eq. (2.28) is redefined as follows by centroid method with threshold [15, 16]:

$$F'(x, y) = \begin{cases} f(x, y) - T & f(x, y) \geq T' \\ 0 & f(x, y) < T' \end{cases} \quad (2.31)$$

Here, T' is the selected threshold. Generally, $T' > T$. The computational equation of modified centroid method is as follows:

$$x_0 = \frac{\sum_{x=1}^m \sum_{y=1}^n F'(x, y)x}{\sum_{x=1}^m \sum_{y=1}^n F'(x, y)}, \quad y_0 = \frac{\sum_{x=1}^m \sum_{y=1}^n F'(x, y)y}{\sum_{x=1}^m \sum_{y=1}^n F'(x, y)} \quad (2.32)$$

This method is to find the centroid of pixels with thresholds greater than T' in the original image, equivalent to the original image minus the background threshold. It can be proved that the centroid method with threshold is of a higher accuracy than the traditional centroid method. When $T' = T$ and the gray distribution $f(x, y)$ is not related to the coordinate values of x and y is the centroid method with threshold equivalent to the traditional centroid method.

(4) Surface Fitting Method

Since images of stars on the photosensitive surface of the image sensor can be approximately viewed as of a Gaussian distribution, a Gaussian surface can be used to fit the gray distribution. The two-dimensional Gaussian surface function can be expressed as follows:

$$f(x, y) = A \cdot \exp \left\{ -\frac{1}{2(1-\rho^2)} \left[\left(\frac{x-x_0}{\sigma_x} \right)^2 - 2\rho \left(\frac{x}{\sigma_x} \right) \left(\frac{y}{\sigma_y} \right) + \left(\frac{y-y_0}{\sigma_y} \right)^2 \right] \right\} \quad (2.33)$$

Here, as scale coefficient, A stands for the size of gray amplitude. It is related to the brightness (magnitude) of stars. (x_0, y_0) stands for the center of Gaussian function, σ_x, σ_y for the standard deviation in the directions of x and y , respectively, and ρ for the correlation coefficient. Generally, take $\rho = 0$ and $\sigma_x = \sigma_y$. The center (central position coordinates of stars) of the Gaussian function can be obtained by the least square method. To facilitate computation, one-dimensional Gaussian curves in the directions of x and y can be used for fitting, respectively.

The one-dimensional Gaussian curve equation is as follows:

$$f(x) = A \cdot e^{-\frac{(x-x_0)^2}{2\sigma^2}} \quad (2.34)$$

Take the logarithm of Eq. (2.34) and the result is as follows:

$$\ln f(x) = a_0 + a_1x + a_2x^2 \quad (2.35)$$

Here,

$$a_0 = \ln A - x_0^2/2\sigma^2, \quad a_1 = x_0/\sigma^2, \quad a_2 = -1/2\sigma^2$$

Fit the points in the direction of x , and coefficients a_0, a_1, a_2 of the above quadratic polynomials can be acquired by the least square:

$$x_0 = -\frac{a_1}{2a_2} \quad (2.36)$$

Equation (2.36) is the x coordinate of the central point.

Similarly, the y coordinate of the central point can be obtained.

2.4.3 Simulations and Results Analysis [17]

To verify the accuracy of various centroiding methods, star spot images can be generated based on digital image simulations introduced in Sect. 2.3. The image size is 20×20 . There is only one star in the image and the central position of the star spot is (10, 10). The radius of PSF can take one pixel, and the background's gray value of the image is 20. To investigate the influences of gray noise and spot image size on positioning accuracy, the standard deviation of gray noise varies from zero to ten and the magnitude from one to six. Simulation experiments use stars of 5.5 Mv as references. The maximum gray value of its peak point just reaches saturation, i.e., 255. Figure 2.13a shows a star image. Its standard deviation of noise is eight, and its radius of PSF is 1.5. Figure 2.13b shows the amplified image of the original star spot.

(1) Influence of Gray Noise on Positioning Accuracy

Assume the actual central coordinates of the star spot are (x_c, y_c) and the measured central coordinates are (x_i, y_i) . The deviation (e_p) of centroiding and the standard deviation (σ_p) are defined as follows:

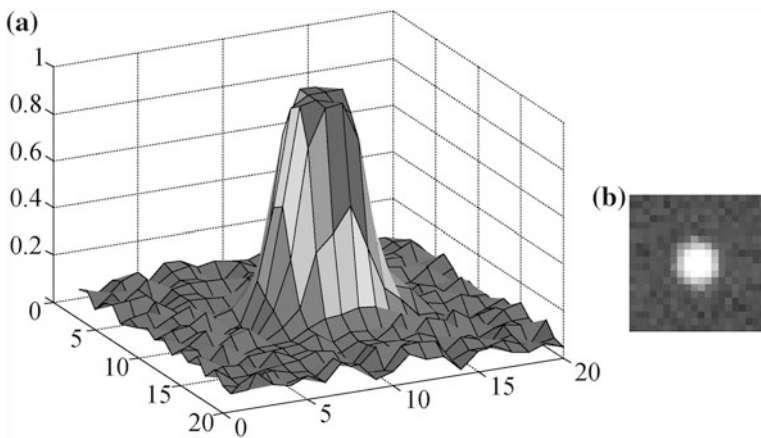


Fig. 2.13 Star images simulated in simulation experiments

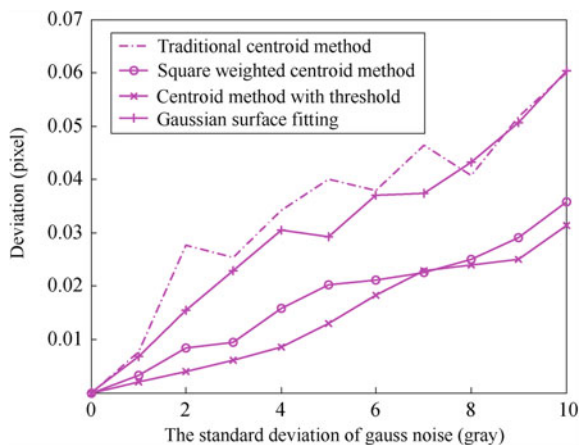
$$e_p = \frac{1}{n} \sum_{i=1}^n \sqrt{(x_i - x_c)^2 + (y_i - y_c)^2}$$

$$\sigma_p = \sqrt{\frac{1}{n-1} \sum_{i=1}^n \left(\sqrt{(x_i - x_c)^2 + (y_i - y_c)^2} - e_p \right)^2} \quad (2.37)$$

Here, $i = 1, \dots, n$, with n for the times of measurements.

The accuracy of various centroiding methods changes with the variance of Gauss noise. The positioning accuracy changes of several centroiding methods are illustrated in Fig. 2.14. It shows the comparison curves when the standard deviation of gauss noise varies from zero to ten. In the simulation experiment, the radius of PSF

Fig. 2.14 Influence of gray noise on positioning accuracy



takes one pixel. Binary threshold T is equal to the background's gray value plus five times the standard deviation of gauss noise. The selected threshold T' of centroid method with threshold is equal to T plus 20 ($T' = T + 20$). Each method undergoes 1000 times of measurements.

The following conclusions can be drawn from the above:

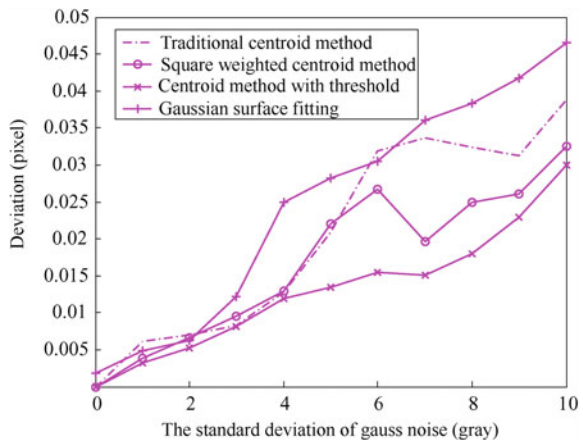
- ① When noise level is low, each method is of high accuracy and the accuracy is nearly the same.
- ② Increase the noise level and the accuracy of various methods decreases. The accuracy decrease of the traditional centroid method is most significant, while the decrease of centroid method with threshold is relatively small.
- ③ The accuracy comparison of various methods is as follows:
centroid method with threshold > square weighting centroid method > Gaussian surface fitting method > traditional centroid method.

(2) Influence of Noise Removal Processing on Positioning Accuracy

As shown in Fig. 2.14, the accuracy of various centroiding methods decreases to varying degrees when the noise level is high. Thus, it is feasible to conduct a low-pass filter processing and then centroiding of star images with noise. And a 3×3 neighborhood average template can be used to conduct low-pass filter processing of images so as to investigate the influence of noise removal on positioning accuracy. After noise removal processing, the deviation comparison curves of various centroiding methods are shown in Fig. 2.15.

By comparing Figs. 2.14 and 2.15, it can be seen that, after a low-pass filter processing, the positioning accuracy of various methods is improved to some degree. Low-pass filter processing can significantly improve the accuracy of traditional centroid methods, but has little impact on other methods. Thus, when other methods are used to conduct centroiding, filter and noise removal in preprocessing can be omitted to save time.

Fig. 2.15 Influence of gray noise on positioning accuracy after noise removal



(3) Influence of Magnitude on Positioning Accuracy

Magnitude determines the size of star spot image. The star spot images (amplified) formed by stars of 6–1 Mv are shown in Fig. 2.16a. Figure 2.16b shows the comparison curves of positioning accuracy obtained by conducting centroiding of the images, respectively. In the experiment, the standard deviation of gray noise is 5.

As shown in Fig. 2.16b, with the increase of magnitude, the positioning accuracy of the centroid method and the modified centroid method is improved, though by not very much. When the Gaussian surface fitting method is used, the deviation

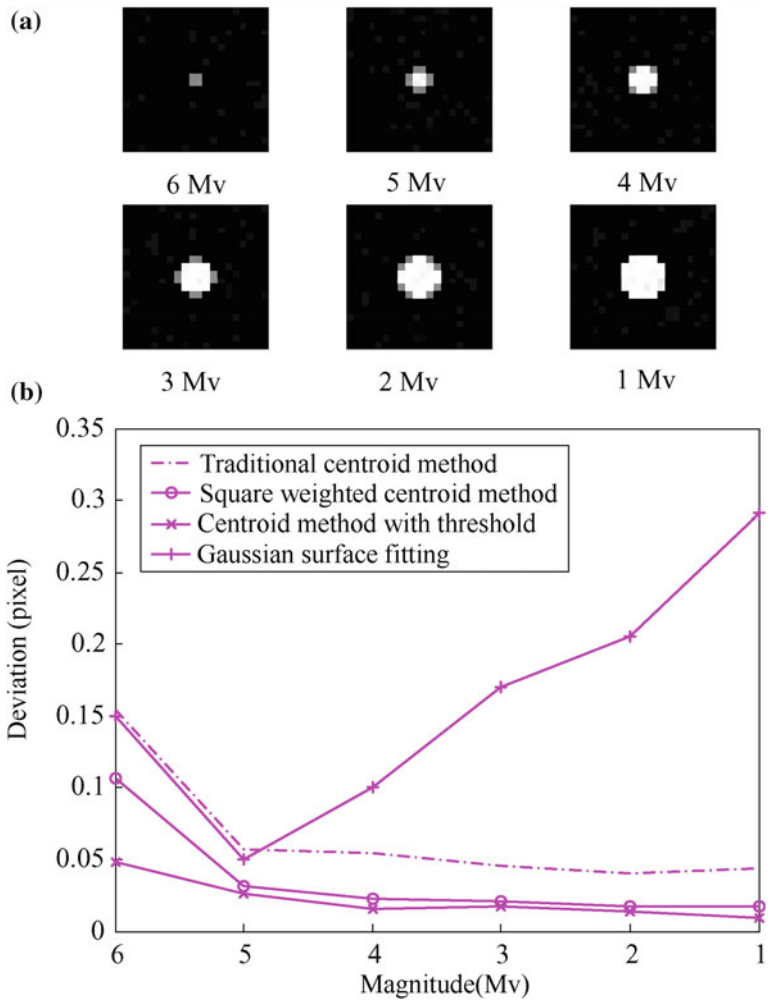
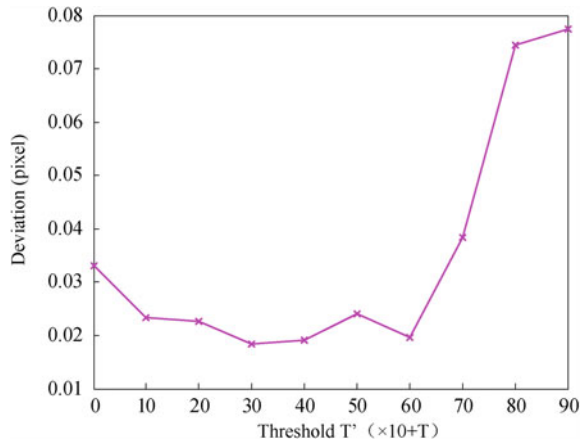


Fig. 2.16 Influence of magnitude on positioning accuracy

Fig. 2.17 Influence of threshold T' on positioning accuracy



first decreases and then increases. The main reason for this is that the gray distribution of star spots reaches saturation and can no longer be fitted through the Gaussian surface. From the above simulations and results analysis, it can be concluded that the centroid method with threshold is a centroiding method that is appropriate for extracting the central positions of star spots. It is of high accuracy and is robust to the influence of noise. In addition, the centroid method with threshold is as simple as the traditional centroid method and is easily implemented.

(4) Selection of Threshold

Threshold T' is an important parameter for the centroid method with threshold, the selection of which affects positioning accuracy. Figure 2.17 shows the variation curve of positioning accuracy with different values of T' . As shown in Fig. 2.17, the positioning accuracy is nearly the same when T' is between $T + 10$ and $T + 60$. Within this range, the deviation reaches a minimum value when T' is approximately $T + 30$.

When the standard deviation of gray noise is 8, $T' = T + 20$, Magnitude = 5, and there is no filter processing, the deviation of the centroid method with threshold is 0.023 pixel and the standard deviation is 0.012 pixel. Thus, it can be concluded that this centroiding method can achieve the positioning accuracy of 0.04–0.05 pixel.

2.5 Calibration of Centroiding Error

The field angle of star is far less than one arc second. Ideally, focus imaging leaves the star spot image of the star sensor within one pixel. To improve the centroiding accuracy of the star sensor, a defocusing technique is often used to make the star spot image spread to a dispersion circular spot. And then the centroid algorithms are

used to compute the center of star spot so as to obtain sub-pixel centroiding accuracy. Currently, the centroiding accuracy of the star sensor can generally achieve $1/10\text{--}2/20$ pixel. To achieve centroiding of higher accuracy, optimization design and noise suppression have to be done for an imaging driving circuit. In addition, based on the characteristics of star imaging and the working characteristics of image device, centroiding error has to be compensated more precisely.

2.5.1 Pixel Frequency Error of Star Spot Centroiding

There are many factors affecting the accuracy of the centroid algorithms, including noise, sampling and quantization errors, etc. These factors, based on their influence form and function, can be put into two categories: those that cannot be compensated and those that can be compensated. Generally speaking, it is very difficult to compensate all kinds of noises (e.g., readout noise, dark current noise, fixed pattern noise, nonuniformity noise, etc.) later in the imaging process. Instead, specific measures are often taken when the image capture circuit is designed to improve the signal-to-noise ratio (SNR) as much as possible. Factors such as sampling and quantization errors have a regular influence on centroiding. In itself, it is an error introduced when an energy distribution center is replaced by a pixel geometric center. This kind of error is often called pixel frequency error. That is, the deviation of the star spot center changes regularly within one pixel [18–20].

(1) Centroiding Deviation Induced by Fill Factor

Generally, pixel fill factor is assumed to be 100% in the centroiding process. In fact, since the pixel fill factor of the image device is less than 100%, nonuniformity of pixel response in space is caused in the quantization process of pixel. Even if there is no noise, pixel quantization will still result in the distortion of PSF and the deviation between the calculated star spot position and its “real” position.

A star spot covering 3×3 pixels (as shown in the circular region of the dotted line) which moves in the direction of the line scanning is illustrated by Fig. 2.18. The dark rectangles in Fig. 2.18 are the regions occupied by transistors of reset, row selection gating, and column amplification. And the surrounding white regions are the effective photosensitive parts of pixels. In the process of scanning, with the changes in pixel photosensitive regions (shaded parts in the circular region of dotted line in Fig. 2.18) covered by the spot, there appears to be a periodical change in the computed spot centroid deviation.

(2) Centroiding Deviation Induced by Charge Saturation

Sampling and quantization errors induced by charge saturation are another important source. When saturation of electron charge occurs in the center pixel of the center energy of star spot, it causes the traditional Gaussian PSF model to be truncated. And the truncation effect induces computational deviation in star spot

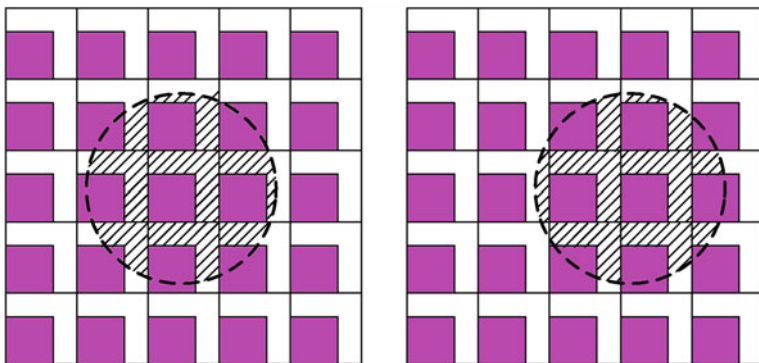


Fig. 2.18 Influence of fill factor on centroiding accuracy

centroid. The truncation of PSF in the direction of X is illustrated in Fig. 2.19. With pixels whose gray value is greater than 255, PSF is then truncated. The truncated Gaussian PSF model is as follows:

$$I(x, y) = \begin{cases} I_0 \exp\left(-\left((x - x_0)^2 + (y - y_0)^2\right)/(2\sigma^2)\right) / (2\pi\sigma^2) & x^2 + y^2 \geq r^2 \\ I_1 & x^2 + y^2 < r^2 \end{cases} \quad (2.38)$$

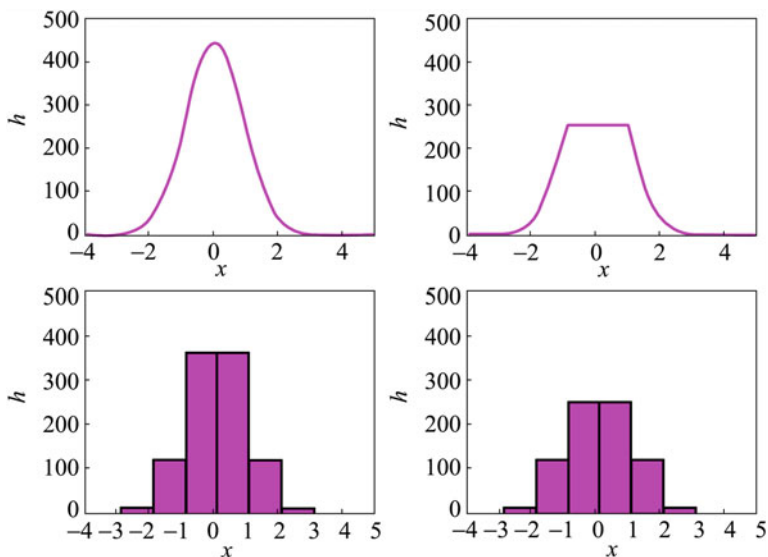


Fig. 2.19 Illustration of Gaussian PSF truncation model induced by charge saturation

Here, I stands for the radiation energy distribution of star spot, x_0 and y_0 for the center of the star spot, x and y for pixel coordinates, and r for the truncation radius. I_0 stands for the total energy of starlight, determined by magnitude. I_1 stands for the saturation value of the electron charge in a pixel. When magnitude is low and starlight is weak, $r = 0$ and this model returns to the original Gaussian PSF.

The common equations of the centroid algorithms are as follows:

$$x_c = \frac{\int \int_A x I(x, y) dx dy}{\int \int_A I(x, y) dx dy}, \quad y_c = \frac{\int \int_A y I(x, y) dx dy}{\int \int_A I(x, y) dx dy} \quad (2.39)$$

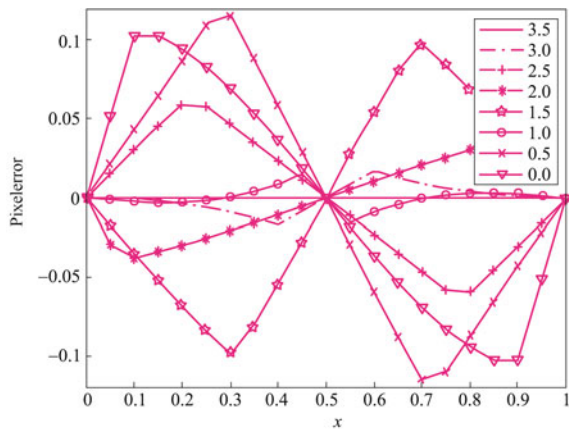
Here, x_c and y_c stand for the radiation center of the star spot, A for the neighborhood of the star spot, x and y for pixel coordinates of image sensor plate, and $I(x, y)$ for radiation distribution function. After discretization of digital images, the computational equations of centroid are as follows:

$$\tilde{x}_c = \frac{\sum_{k=1}^n x_k I_k}{\sum_{k=1}^n I_k}, \quad \tilde{y}_c = \frac{\sum_{k=1}^n y_k I_k}{\sum_{k=1}^n I_k} \quad (2.40)$$

Here, \tilde{x}_c and \tilde{y}_c stand for the center of star spot after discretization, n for the number of pixels with a gray value greater than threshold T' , k for the index number of pixels, x_k and y_k for the coordinates of the k -th pixel, and I_k for the gray output of the k -th pixel.

Figure 2.20 shows the pixel frequency error curves induced by charge saturation obtained through simulations with different magnitudes when there is no noise. The directions of x and y are mutually independent, and here the error in the direction of x is simulated. As shown in Fig. 2.20, the deviation within pixels approximately follows the sine function. But with the changes of magnitude, from 3.5 to 0.0 Mv, both the amplitude and phase change.

Fig. 2.20 Centroiding pixel frequency error of star spots with different magnitudes induced by charge saturation



2.5.2 Modeling of Pixel Frequency Error

Next, with the star of 0 Mv as reference, the pixel frequency error model of the centroid algorithms is introduced, and brightness and positional noise are increased to simulate and compute pixel frequency error. First, the pixel frequency error of the model built is as follows:

$$\begin{cases} E_x = A_x(\sin(2\pi x_p + 2\pi B_x) - \sin(2\pi B_x)) \\ E_y = A_y(\sin(2\pi y_p + 2\pi B_y) - \sin(2\pi B_y)) \end{cases} \quad (2.41)$$

Here, A_x and A_y stand for the deviation amplitude coefficients in the directions of x and y , B_x and B_y for deviation phase coefficients, and x_p and y_p for position coordinates within one pixel. Since the pixel of the image sensor is square shaped, assume $A_x = A_y$ and $B_x = B_y$. And for the same magnitude, the deviation amplitude coefficient and phase coefficient are constants. Here, use the direction of x as reference, and the parameter estimation in the direction of y can be processed in the same way.

Using least square estimation, the estimation equations of amplitude and phase deviations are as follows:

$$\begin{cases} \Delta E_x = [\sin(2\pi x_p + 2\pi B_x), \quad 2\pi \cos(2\pi x_p + 2\pi B_x) - 2\pi \cos(2\pi B_x)] \begin{bmatrix} \Delta A_x \\ \Delta B_x \end{bmatrix} \\ \Delta E_y = [\sin(2\pi y_p + 2\pi B_y), \quad 2\pi \cos(2\pi y_p + 2\pi B_y) - 2\pi \cos(2\pi B_y)] \begin{bmatrix} \Delta A_y \\ \Delta B_y \end{bmatrix} \end{cases} \quad (2.42)$$

Here, ΔE_x and ΔE_y stand for the measured values of pixel deviation in the directions of x and y , ΔA_x and ΔB_x for pixel frequency error amplitude and phase estimation in the direction of x , and ΔA_y and ΔB_y for pixel frequency error amplitude and phase estimation in the direction of y .

2.5.3 Calibration of Pixel Frequency Error

The basic parameters of the simulation star sensor are as follows:

FOV: $12^\circ \times 12^\circ$

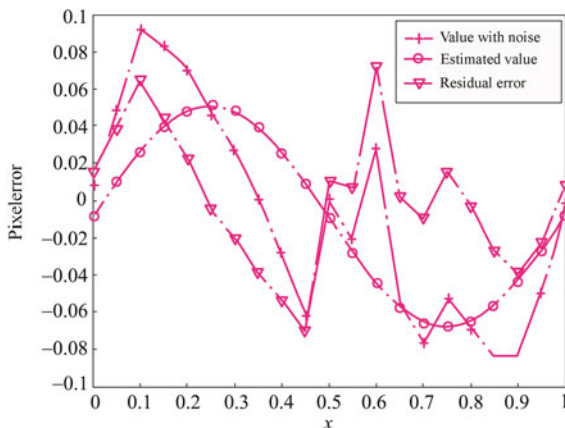
pixel array: 1024×1024

pixel size: $0.015 \text{ mm} \times 0.015 \text{ mm}$

focal length: 73.03 mm .

Assume the random error of the central position of the star spot within pixels is Gaussian white noise with mean = 0 and mean square deviation = 0.01 pixel. The

Fig. 2.21 Calibration of pixel frequency error



brightness error is also Gaussian white noise and its mean square deviation is 2% of the saturated gray value. The threshold takes five times the mean square deviation of brightness, i.e., 10% of the saturated gray value. Figure 2.21 shows the calibration results of pixel frequency error. ‘+’ stands for the simulation value with noise, ‘O’ for sine estimated value, and ‘Δ’ for residual error.

The amplitude of sine deviation after calibration is 0.060 pixel and the phase is $1.4 \times 10^{-3} \text{ rad}$. The mean root of the simulation value’s error is 0.055 pixel, and the mean root of residual error after calibration is 0.036 pixel. The computation accuracy of star spot centroid is improved by 34%, which shows the calibration value is of remarkable accuracy. It is worth noting that the above simulations are based on the star of 0 Mv. The pixel frequency error of each magnitude is different. Thus, to fully calibrate the pixel frequency errors of all magnitudes to be dealt with by the star sensor, the amplitude and phase of several major magnitudes’ pixel frequency error can be measured, and then interpolation can be used to calibrate the centroiding results of different magnitudes.

In the laboratory, the starlight simulator and a turntable of high accuracy can be used to calibrate the pixel frequency error of centroiding. As shown in Fig. 2.22, the turntable is adjusted to leave the central positions of the imaging star spot on the edge of pixels to reduce possible interferences in the direction of y . The turntable begins from the initial position of pixel x . Its rotation angle from pixel x to pixel $x + 1$ is approximately 0.05 pixel each interval. In the process, 21 points are



Fig. 2.22 Sampling within a pixel

sampled. Conduct multiple samplings (100 times) at each point to reduce random error. Repeat the sampling process in the direction of y . To obtain a more precise estimated parameter value of pixel frequency error, five pixels can be selected in the up, down, left, right, and middle parts of the star sensor's image sensor plate to repeat the above data collection. The parameters can be integrated to solve the amplitude and phase deviation coefficients. For example, for captured image of resolution 1024×1024 , the sampling of pixel frequency error can be done at five pixel points, i.e., (127, 512), (512, 512), (896, 512), (512, 127), (512, 896), respectively.

References

1. Liebe CC (2002) Accuracy performance of star trackers - a tutorial. *IEEE Trans Aerosp Electron Syst* 38(2):587–599
2. Jeffery WB (1994) On-orbit star processing using multi-star star trackers. *SPIE* 2221:6–14
3. Ju G, Kim H, Pollock T et al (1999) DIGISTAR: a low-cost micro star tracker. *AIAA Space Technology Conference and Exposition*, Albuquerque, AIAA: 99-4603
4. Chen Y (2001) A research on three-axis attitude measurement of satellites based on star sensor. Doctoral Thesis of Changchun Institute of Optics, Fine Mechanics and Physics, Chinese Academy of Sciences, Changchun
5. Wei X (2004) A research on star identification methods and relevant technologies for star sensor (pp 15–43). Doctoral Thesis of Beijing University Aeronautics and Astronautics, Beijing
6. Zhang G, Wei X, Jiang J (2006) Star map identification based on a modified triangle algorithm. *Acta Aeronautica et Astronautica Sinica* 27(6):1150–1154
7. Wang X (2003) Study on wild-field-of-view and high-accuracy star sensor technologies. Doctoral Thesis of Changchun Institute of Optics, Fine Mechanics and Physics, Chinese Academy of Sciences, Changchun
8. Weng JY (1992) Camera calibration with distortion models and accuracy evaluation. *IEEE Trans Pattern Anal Mach Intell* 14(10):965–980
9. Yuan J (1999) Navigation star sensor technologies. Doctoral Thesis of Sichuan University, Chengdu
10. Zhang Y (2001) Image segmentation. Science Press, Beijing
11. Hao X, Jiang J, Zhang G (2005) CMOS star sensor image acquisition and real-time star centroiding algorithm. *J Beijing Univ Aeronaut Astronaut* 31(4):381–384
12. Grossman SB, Emmons RB (1984) Performance analysis and optimization for point tracking algorithm applications. *Opt Eng* 23(2):167–176
13. Zhou R, Fang J, Zhu S (2000) Spot size optimization and performance analysis in image measurement. *Chin J Sci Instrum* 21(2):177–179
14. Shortis MR, Clarke TA, Short TA (1994) Comparison of some techniques for the subpixel location of discrete target images. *SPIE* 2350:239–250
15. Sirkis J (1990) System response to automated grid methods. *Opt Eng* 29(12):1485–1491
16. West GAW, Clarke TA (1990) A survey and examination of subpixel measurement techniques. *SPIE* 1395:456–463
17. Wei X, Zhang G, Jiang J (2003) Subdivided locating method of star image for star sensor. *J Beijing Univ Aeronaut Astronaut* 29(9):812–815
18. Giancarlo R, Domenico A (2003) Enhancement of the centroiding algorithm for star tracker measure refinement. *Acta Astronaut* 53:135–147

19. Ying JJ, He YQ, Zhou ZL (2009) Analysis on laser spot locating accuracy affected by CMOS sensor fill factor in laser warning system. The ninth international conference on electronic measurement and instruments (pp 202–206) (2)
20. Hao X (2006) CHU key technologies of miniature CMOS star sensor (pp 61–64). Doctoral Thesis of Beijing University Aeronautics and Astronautics, Beijing

Star Identification

Methods, Techniques and Algorithms

Zhang, G.

2017, XI, 223 p. 162 illus., 144 illus. in color., Hardcover

ISBN: 978-3-662-53781-7